

which is coincident with the tomographic line 1 shown in Figure 11a. The topographic line has been merged on the tomogram and the total information is visible in Figure 15b. The visual analysis shows the surface tomogram overlapping almost perfectly with the topographic line, which is represented by yellow line 1.

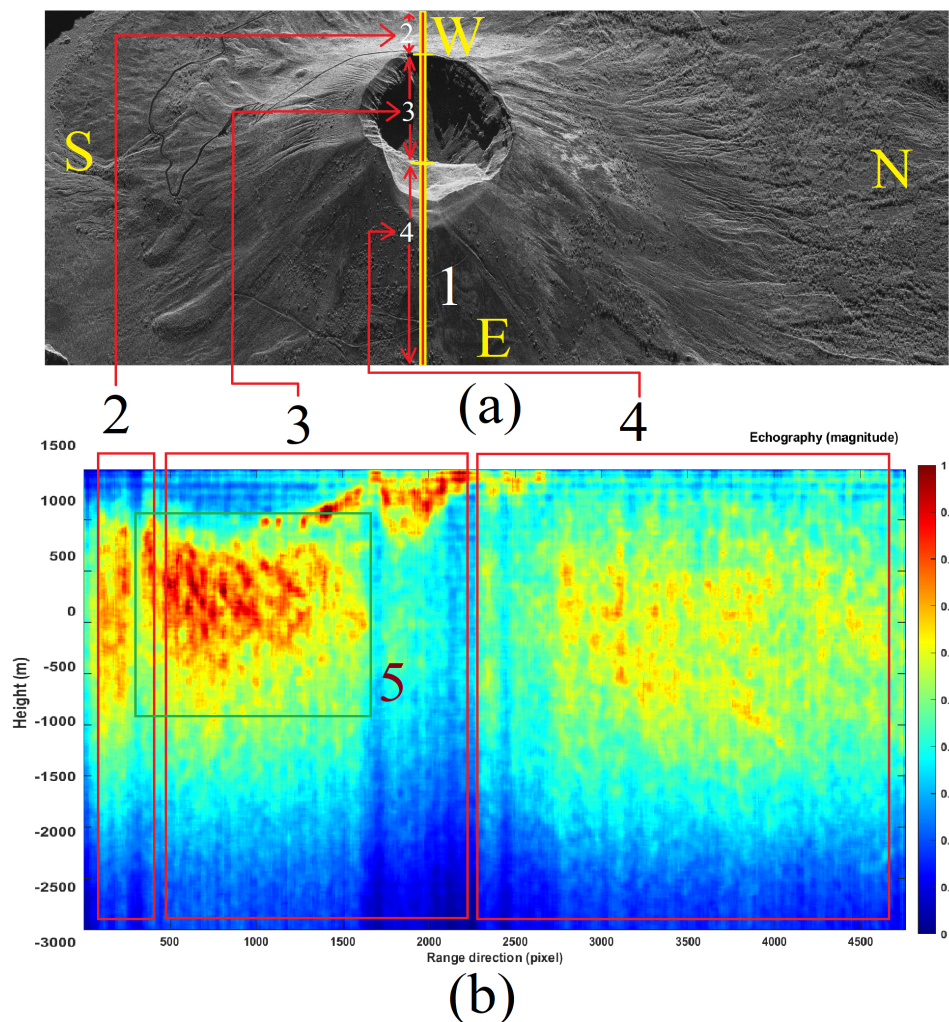


Figure 14. Tomographic results and analysis. (a) SLC SAR data of Vesuvius. (b) Tomographic results and analysis.

The next validation case is to compare the position of the topographic line 1 visible in Figure 16a (always extrapolated from the SRTM-DEM) with the top of the tomography coincident to line 1 shown in Figure 8a and the consequent merged information is visible in Figure 15b. The visual analysis shows the almost perfect overlap of the superficial component of the tomogram with the topographic line, which is represented by yellow line 1. The last performance analysis case study is shown in Figure 14a,b. For this case, the tomographic line is perfectly oriented along the range direction. The objective was to study the tomographic reconstruction robustness under heavy foreshortening and layover effects. The tomographic picture is reported in Figure 14b. In this case, the eastern side of the crater (the one characterized by layover) is better seen than the western side (the one characterized by foreshortening). However, possible magmatic fluid conduits communicating with both the inner and outer parts of the main volcano cone remain visible on the eastern side of the crater. The tomogram has been divided into three portions: result numbers 2, 3, and 4, which are compartmentalized by three red squares visible in Figure 14b. Each tomographic surface is pointed at its tomographic line reference, which is visible in Figure 14a. The portion of the tomogram characterized by layover is number 2, while result number 3 is

the one representing the interior of the main crater. Finally, result number 4 refers to the descending side of the volcanic cone. Results confirm the presence of vibratory material, similar to rock, probably composed of cooled compact solidified magma that produces a substantial blockage mass located deeply inside the main volcanic conduit. This blockage is visible within box 5 of Figure 14b.

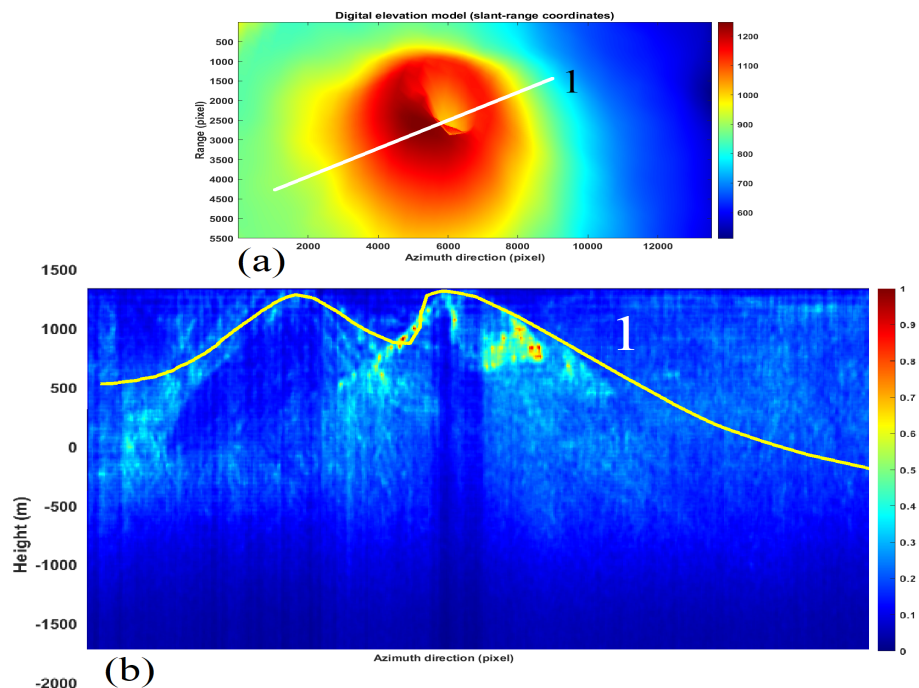


Figure 15. Range-line echographic tomography result (magnitude), and validation through DEM. (a) DEM result in the slant-range coordinates. (b) Tomographic result (in magnitude), and topographic height (yellow line taken from the white line 1 of Figure (a)).

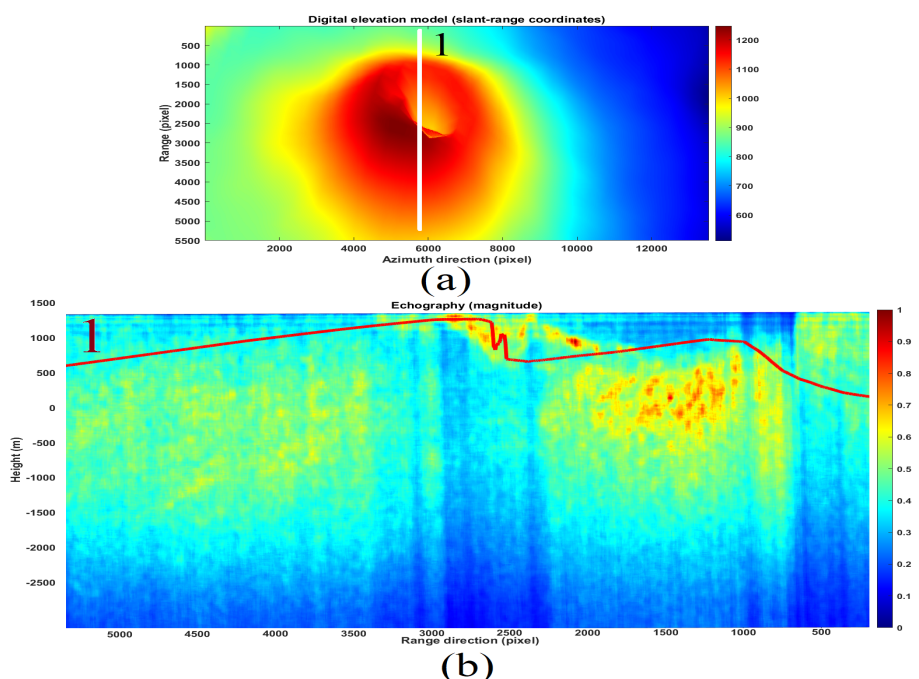


Figure 16. Range-line echographic tomography result (magnitude), and validation through DEM. (a) DEM results in the slant-range coordinates. (b) Tomographic map (in magnitude), and topographic height (yellow line). The result is calculated over the white line drawn on the DEM reported in Figure (a). The yellow tomographic line is indicated by the number 1.

4.2. Vibration Validation

Vibrational validation is carried out by comparing data estimated by the satellite with those observed by the “in situ” seismological stations installed at Vesuvius. In situ data are provided in open source from the Italian National Institute of Geophysics and Volcanology (INGV), and are downloadable from the following website: <https://eida.ingv.it/it/>, accessed on 23 April 2022. In this context, the vibrational data estimated by the satellite and those provided by the seismic in situ stations listed in Table 2 are synchronized in space and time.

Table 2. Characteristics of the “in situ” seismographs.

“In-Situ” Station	Network	Channel	Location (Lat, Lon)
Vesuvius-East Crater	IV-VCRE	HH	40.81899°, 14.431419°
Vesuvius-North Bunker	IV-VBKN	HH	40.829959°, 14.429881°

Figure 17 shows the map where the Vesuvius seismic stations are located. IV-VCRE and VBKN in situ station data are considered in this stage and are the only ones compatible with line-of-sight radar visibility. All other measurement stations were either not visible or were located outside the SAR imaging scene. Figures 18a,b and 19a,b represent the optical and radar observations, respectively, of the seismographic stations. The first facility is located at the east side of the crater and the second one is installed toward the northern side. The two stations are successfully represented on both the optical and radar images (indicated both by arrows number 1). In Figure 20a–c, the vibrational spectrum streaming recorded by the IV-VCRE seismographic station, superimposed to the respective spectrogram recorded by radar, is depicted. Figure 20a represents the unfiltered full-bandwidth spectrum, while Figure 20b is the filtered spectrum; finally Figure 20c represents a narrowed detail spectrum at approximately 1 kHz of bandwidth. The blue color function is that of the “in situ” station, while the brown color function is the radar-estimated vibrational spectrum. The native time trend (1 s of synchronized streaming) is shown in Figure 21a. The filtered time-domain plot (approximately composed of 1-s wide synchronized data streaming) is reported in Figure 21b, finally the IV-VCRE in situ station versus SAR vibrational streaming measurement errors is proposed in Figure 21c. The blue function represents the unfiltered error, while the one in brown is the filtered error. It can be seen that this error, while oscillating around zero, remains confined to very low values. In Figure 22a–c, the spectrum of the vibrational streaming recorded by the IV-VBKN seismographic station is represented. Figure 22a represents the spectrum in its entirety, Figure 22b is the filtered spectrum, while Figure 22c represents a narrowed detail dataset at approximately 1 kHz of bandwidth. Also, in this case the blue and the brown functions are the in situ and the radar estimated vibrational spectrum, respectively. The unfiltered time-domain sampled vibrations (approximately 1-s synchronized streaming) are shown in Figure 23. Although it is very difficult to perfectly synchronize two different measurement instruments—the first one is located on the ground, while the second one is located in space—such time synchronization turns out to be very acceptable. Both instruments measure the seismic background of the area. This result brings the SAR’s effective measurement accuracy to attention.

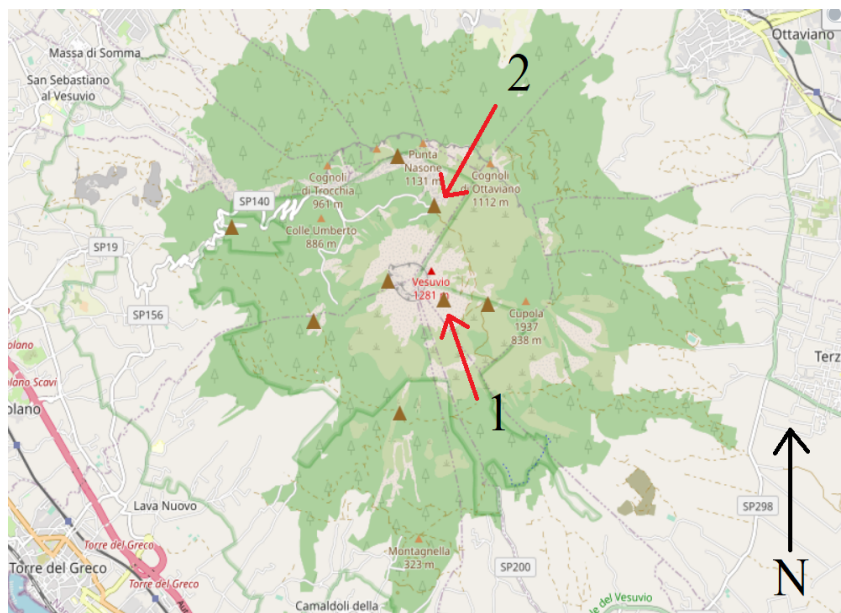


Figure 17. “In situ” seismograph stations.

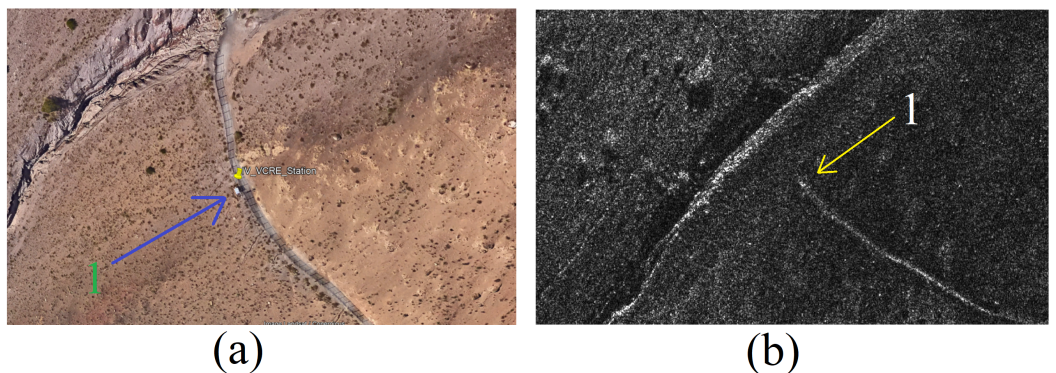


Figure 18. IV-VCRE seismograph station, located on the east side of the crater. (a) Optical image. (b) SAR image.

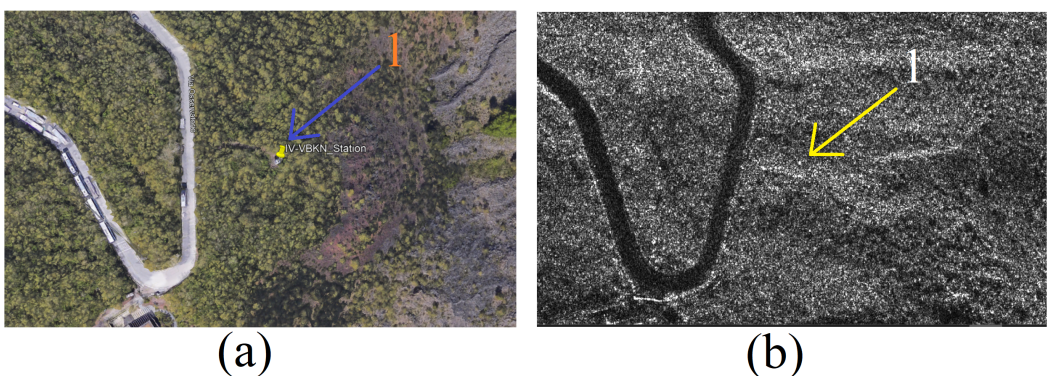


Figure 19. IV-VBKN seismograph station, located on the north side of the crater. (a) Optical image. (b) SAR image.

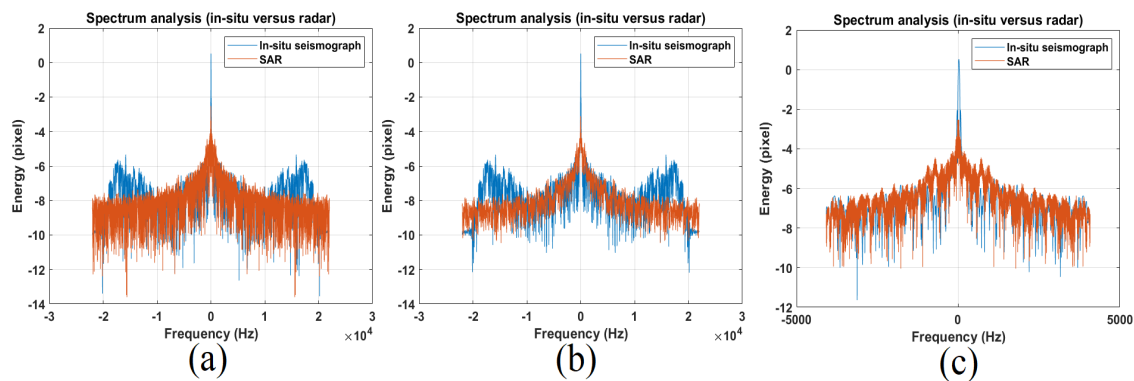


Figure 20. IV-VCRE seismograph station versus SAR frequency-domain vibrational streaming. (a) Native (b) low-pass filtered. (c) Narrow-band particular.

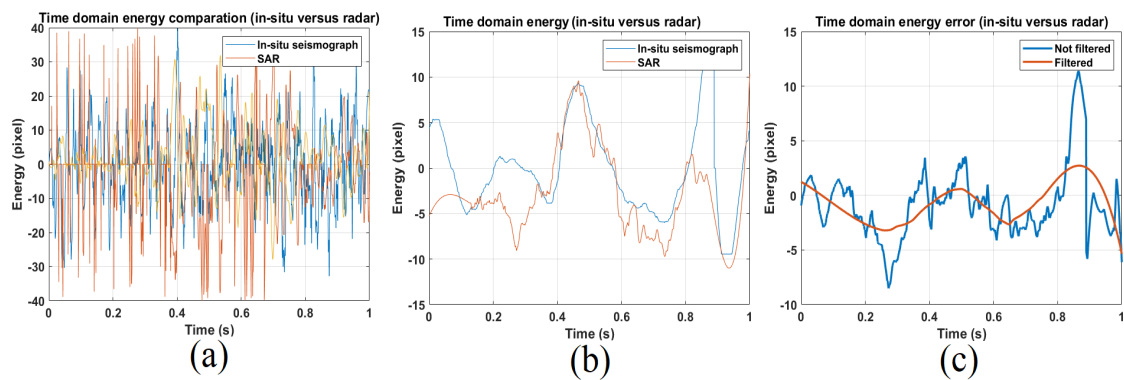


Figure 21. IV-VCRE seismograph station versus SAR synchronized time-domain vibrational streaming. (a) Native (b) low-pass filtered. (c) errors.

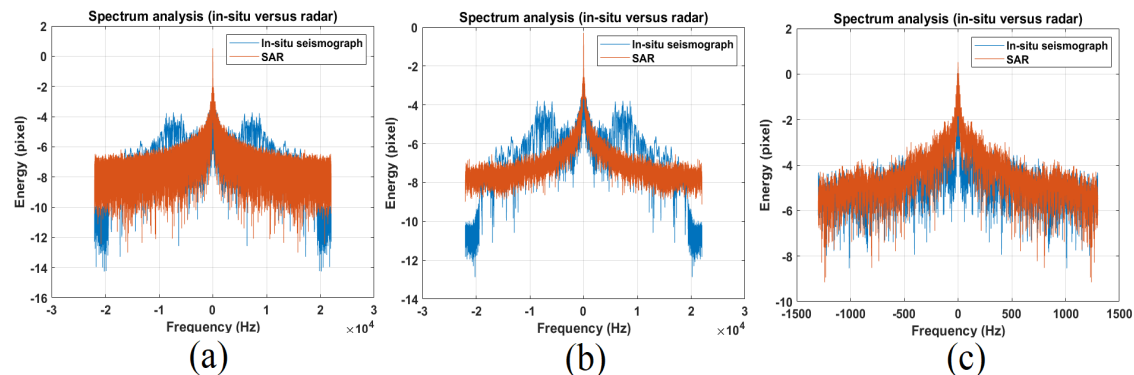


Figure 22. IV-VCRE seismograph station versus SAR synchronized signals spectrum. (a) unfiltered. (b) low-pass filtered. (c) 1 kHz filtered particular.

4.3. Tomographic Validation

In this section, the comparison of data estimated through magnetotelluric tomography with those estimated through SAR tomography is evaluated. Successively, the visual comparison relates the magnitude of the earthquakes that occurred during the month, within which the SAR observation is made. The estimated tomographic planes found the perfect overlap of the estimated results with the radar. In Figure 24a–d, we report the radar-estimated tomographic maps superimposed on the magnetotelluric tomography results. More precisely, Figure 24a is the in-range SAR tomography; Figure 24c is the superposition of Figure 24a radar tomography with magnetotelluric tomography. On the other hand, Figure 24b shows the range-azimuth oblique SAR tomography, while

Figure 24c is the superposition of the oblique radar tomography in Figure 24b with the magnetotelluric tomography. In Figure 25a,i, some details are depicted to better show the existing tomographic overlay. The images in Figure 25a–c refer to the topographic detail of Figure 24a, where a reference area is indicated by arrow number 1. Figure 25a is the radar data alone, Figure 25b is the 50% overlay of the radar data on the magnetotelluric tomography, and finally Figure 25c is the magnetotelluric tomography map shown alone. The images of Figure 25d–f refer to the tomographic detail of Figure 24b, indicated by arrow 2. Figure 25d is the radar data alone, Figure 25e is the 50% overlay of the radar data with the magnetotelluric tomography, and finally Figure 25f is the magnetotelluric tomography, again shown alone.

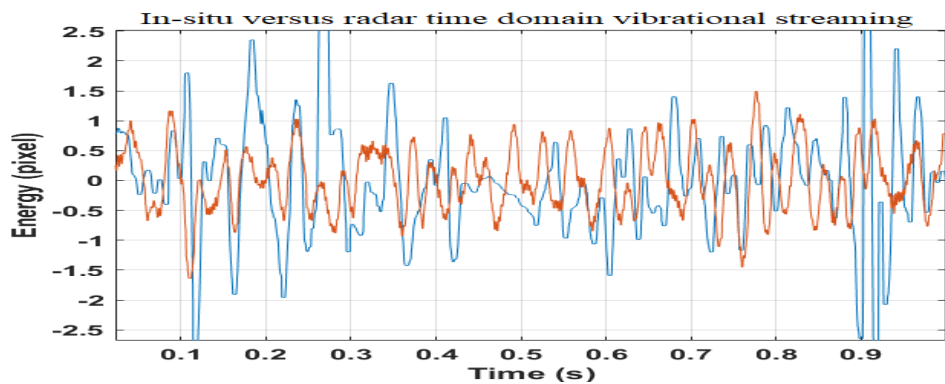


Figure 23. IV-VCRE seismograph station versus SAR synchronized time-domain vibrational streaming.

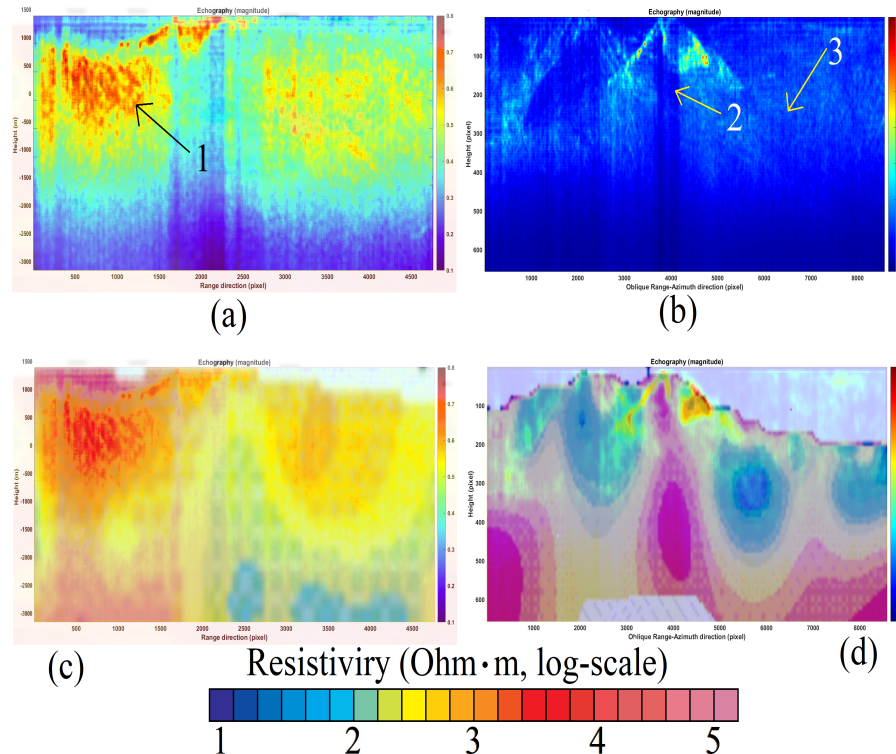


Figure 24. Overlay of SAR Doppler tomography with magnetotelluric tomography. (a,b) tomographic results. (c,d) Tomographic versus resistivity tomography results. The resistivity scale refers to captures (c,d). The symbol · represents the scalar multiplication.

Finally, the images of Figure 25g–i refer to the tomographic detail of Figure 24b, indicated by arrow 3. Figure 25g is the radar data alone, Figure 25h is the 50% overlay of the radar data with the magnetotelluric tomography, and finally Figure 25i is the magnetotelluric tomography without any overlay. The comparative assessment formed by the

visual validation between the results estimated through the seismic sensors network installed in the proximity of Vesuvius and measured satellite results are secondly performed. The data were extrapolated from the public and institutional websites of the INGV. In this context, the seismic values map is shown in Figure 26, and is correlated to the SAR tomographic results of Figure 14b. In the Figure, blue and colored circles represent some seismic events. The center of each point is placed in the 3D space on which the source of the seismic event was measured, while the radius of each circle measures its magnitude. The Figure also contains the magnitude legend and four scales can be distinguished, the number 0 value represents all seismic events between 0 and 1 Richter scale magnitude. Number 1 represents all events of magnitude between 1 and 2, circle 2 between 2 and 3, and finally, the largest circle is the number 3, which represents all seismic events greater than 3 degrees of magnitude on the Richter scale. The blue circles represent seismic events that occurred throughout January 2022, while the red color represents only those seismic events that occurred in February 2022, which is the month in which the SAR data was acquired. From a visual comparison, we keep a good correspondence of the data if compared to the one estimated through SAR tomography. It is clear that the temporal correspondence of the SAR acquisition which consists of a few seconds is not comparable with the large temporal duration of the measurements made through the “in situ” sensors, but we find a good correlation between the red seismic events that coincide very much in space with the magmatic consistency estimated through the SAR seismic tomography. The depth also coincides greatly.

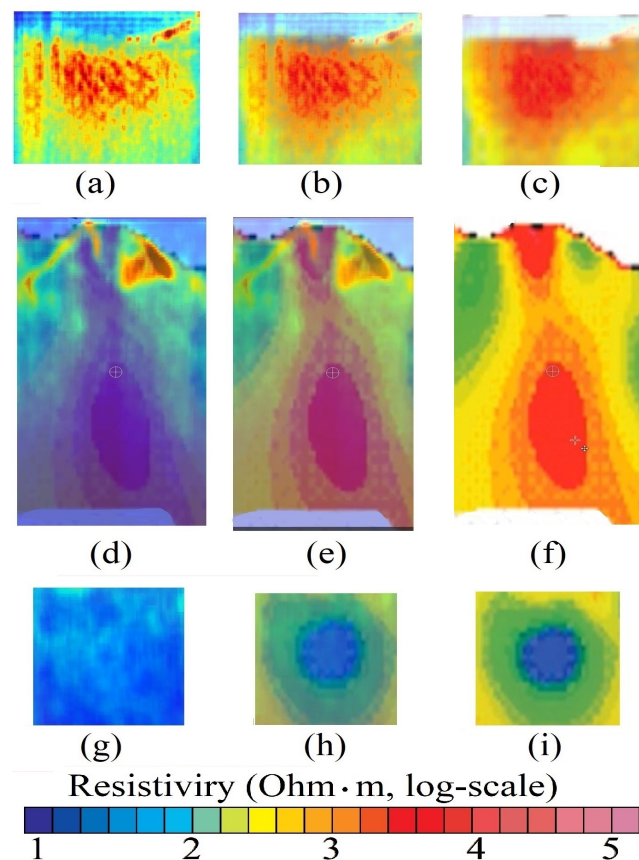


Figure 25. Overlay of SAR Doppler tomography with magnetotelluric tomography (particulars). (a,d,g) Radar tomographic results. (b,e,h) Radar tomographic results 50% overlapped to magnetotelluric tomographic results. (c,f,i) Magnetotelluric tomographic results. The symbol · represents the scalar multiplication.

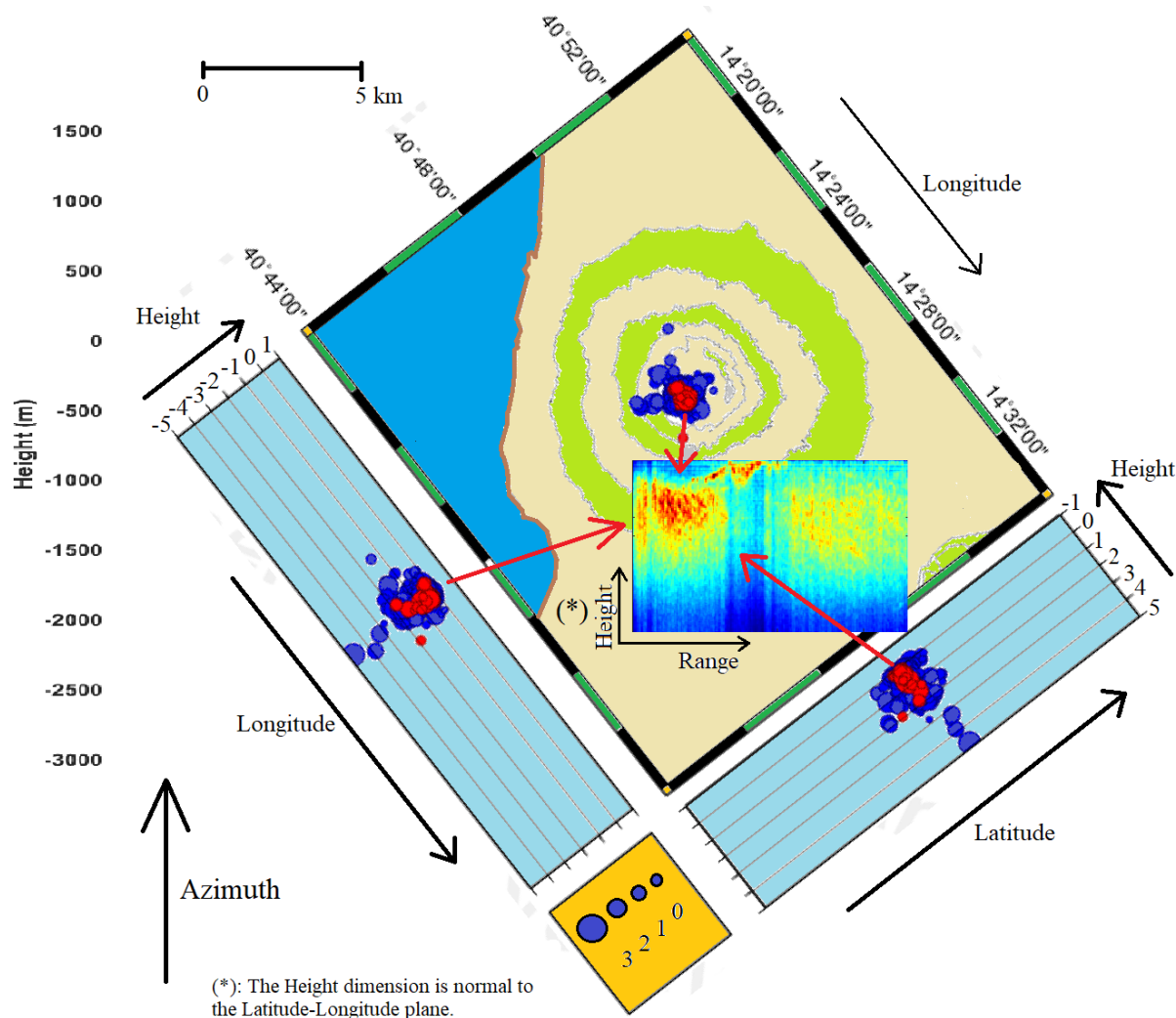


Figure 26. Cartographic representation of the seismic events that occurred during the year 2022 at Vesuvius. The pegs represent the position in which one actually occurred in 3D space (latitude-longitude and depth), the radius the magnitude. The red roundels represent those that occurred the month where the SAR acquisition was taken. The magnitude legend has four scales of earthquake in the Richter scale, from the smallest (0 to 1) to the largest (greater than 3).

5. Discussion

This is the first time that a SAR has been employed to estimate the consistency of depth structures, down to 3 km, considering also that the observations are performed from space. This preliminary work may pave the way for a new type of radar exploitation, where the carrier physical phenomenon is formed by coherent electromagnetic X-band transmissions and azimuth focusing made using ad hoc designed matched filters tuned at the zero Doppler. This procedure can grab phononic (intended to be the vibration of matter) physical parameters. In this context, photons are used as a carrier medium that contains phononic information as well. It seems that this system, although still to be improved and refined, works. This technique can be extended to maybe detect crude oil, or natural gas underground pockets, to quickly search for veins in metals and rare earth, or to assess the consistency of the matter from which all the world's great infrastructures are made. In the present work, we first thought about both nature and humanity preservation, and then found a method (which at present remains unresolved), namely that of looking inside volcanoes with high-resolution imaging from space. It seemed natural to us to focus our research on one of the world's most dangerous volcanoes. It is located in Italy in the middle of the highly populated city of Naples, Vesuvius. In addition, this technique

allows the construction of an accurate and truthful model of the Earth's subsurface. This possibility appears very important and could serve in helping to strengthen predictive models useful in both the volcanological and seismological fields. According to [34], there is an electromagnetic interaction with the atmosphere. The technique employs the single SAR image, acquired in a time of about 14 s; surely there is an electromagnetic phase delay due to the atmosphere. However, this delay, in practice, does not affect the correct estimation of the tomography, as it is constant in time (this effect is assumed to be time-invariant), so we assume that atmospheric delay remains constant within the SAR acquisition. However, the proposed technique is very robust in terms of compensating for atmospheric interaction as we scan in the Doppler domain, within the single SAR image. To this end, MCA of atmospheric issues is fully described and solved in [28]. Concluding, the proposed technique, can be considered a potential "gap-filler", thus allowing us to look inside rigid bodies, like volcanoes, even over high spatial resolution. Authors employed specifically designed software for processing tomographic slices. At the present, there is no commercial software capable of extracting the phonon information embedded in the SAR data. The authors are available in collaborating with other research groups for reproducing the proposed tomographic method specifically, for all those sites that need to be studied in depth.

6. Conclusions

This work describes an imaging method based on the analysis of micro-motions present on volcanoes and generated by underground Earth tremors. We showed a series of tomographic maps representing the internal echography of volcanoes. Processing the coherent vibrational information present on the single SAR image, in the single-look-complex configuration, we exploited the sound information penetrating tomographic imaging over a depth of about 3 km from the Earth's surface. The experimental results were calculated processing an SLC image from the COSMO-SkyMed Second Generation satellite constellation of the Italian volcano Vesuvius. Tomographic maps revealed the presence of the solidified magma, and the main and the secondary feeder conduit. In addition, both the main and secondary fractures are visible. Concluding, we also declare that although the results of the considered case study are promising, they should be confirmed by using other case studies in the future.

Funding: This research received no external funding.

Data Availability Statement: Data used for this work can be requested at <https://www.e-geos.it/> or <https://www.asi.it/> (accessed on 1 April 2022).

Acknowledgments: We would like to thank Daniele Perissin for making the SARPROZ software available, through which many calculations were carried out more easily and quickly. We also thank the Italian Space Agency for providing the SAR data. The in situ seismic numerical data were kindly provided by the Italian Institute of Geophysics and Volcanology (INGV), which can be downloaded from the website: <https://eida.ingv.it/> (accessed on 23 April 2022). Finally, We thank Corrado Malanga, Professor of Industrial Chemistry at the Faculty of Chemistry, University of Pisa (Italy), for guiding me in formulating the idea of extrapolating phononic information through photonic processing of SAR data. (<https://corrdomalangaexperience.com/>, accessed on 1 January 2022).

Conflicts of Interest: The author declare no conflict of interest.

Appendix A. Mathematical Formulation

Appendix A.1. Doppler Sub-Apertures Model

The SAR data belonging to the electromagnetic image are formed through the focusing process that involves the application of a two-dimensional matched filter acting in the

range direction and in the azimuth direction. The SLC signal resulting from compression is given by [35]:

$$s_{SLC}(k, x) = 2N\tau \exp\left[-j\frac{4\pi}{\lambda}r\right] \text{sinc}\left[\pi B_{cr}\left(k - \frac{2R}{c}\right)\right] \text{sinc}[\pi B_{cD}x] \quad (\text{A1})$$

for $x = kt$, $k = \{0, 1, \dots, N-1\}$, $x = \{0, 1, \dots, M-1\}$, with $N, M \in \mathbb{N}$.

Equation (A1) represents the focused SAR signal generated by the back-scattered electromagnetic energy of a point target supposed to be stationary. The parameter λ is the SAR radio-frequency wavelength. The terms B_{cr} , and $B_{cD} = \frac{4Nd}{\lambda r}$ are the total chirp and Doppler bandwidths respectively. The total synthetic aperture is equal to $L_{sa} = 2Nd$ and the azimuth resolution $\delta_D \approx \frac{1}{B_{cD}} = \frac{\lambda R}{2L_{sa}}$. In (A1) the $\frac{2R}{c}$ parameter identifies the position in range where the maximum of the sinc function is positioned, while in azimuth it is centered around "zero". In the case where the peak of the sinc function has a nonzero coordinate along the azimuth dimension, Equation (A1) can be recast as:

$$s_{SLC}(k, x) = 2N\tau \exp\left[-j\frac{4\pi r}{\lambda}\right] \text{sinc}\left[\pi B_{cr}\left(k - L_{cg}\right)\right] \text{sinc}[\pi B_{cD}(x - L_{Dh})] \quad (\text{A2})$$

for $L_{cg}, L_{Dh} \in \mathbb{R}$,

in (A2) L_{cg} , and L_{Dh} are the slant-range, azimuth position of the single-target beam center, into the image coordinates. In this context the DFT is equal to:

$$\begin{aligned} S_{SLC_F}(n, q) &= \text{DFT2}\left\{2N\tau \exp\left[-j\frac{4\pi r}{\lambda}\right] \text{sinc}[\pi B_{cr}k] \text{sinc}[\pi B_{cD}x]\right\} \\ &= 2N\tau \exp\left[-j\frac{4\pi r}{\lambda}\right] \sum_{k=0}^{N-1} \sum_{x=0}^{M-1} \text{sinc}[\pi B_{cr}n] \text{sinc}[\pi B_{cD}q] \\ &\quad \exp\left(-j\frac{2\pi kn}{N}\right) \exp\left(-j\frac{2\pi xq}{M}\right) \\ &= 2N\tau \exp\left[-j\frac{4\pi r}{\lambda}\right] \frac{1}{\pi B_{cr}} \text{rect}\left[\frac{n}{\pi B_{cr}}\right] \frac{1}{\pi B_{cD}} \text{rect}\left[\frac{q}{\pi B_{cD}}\right] \\ &\quad \exp\left(-j2\pi nL_{cg}\right) \exp\left(-j2\pi qL_{Dh}\right), \end{aligned} \quad (\text{A3})$$

which has a rectangular shape. In (A3) the parameter DFT2 is the two-dimensional digital Fourier transform.

Appendix A.2. Doppler Sub-Apertures Model

In this paper author tests a strategy that employs Doppler sub-apertures, that are generated to measure target motion. Figure 2 represents the used bandwidth allocation strategy. From the single SAR image We calculate the DFT2 which, according to (A3), has a rectangular shape. As can be seen from Figure 2, B_{cD} is the total Doppler band synthesized with the SAR observation, while $B_{DL} = \frac{B_{cD}}{2}$ is the bandwidth not processed from the matched-filter boundaries, to obtain a sufficient sensitivity to estimate target motions. In this context formula (A3) is the focused SAR spectrum, at maximum resolution, thus exploiting the whole band $\{B_{cr}, B_{cD}\}$, in accordance with the frequency allocation strategy shown in Figure 2, the following range-Doppler sub-apertures large-matrix is constructed for the Master multi-dimensional information:

$$S_{SLC}(k, x)_M = \begin{bmatrix} S_{SLC}(k, x)_{M_{\{1,1\}}} & S_{SLC}(k, x)_{M_{\{1,2\}}} & S_{SLC}(k, x)_{M_{\{1,3\}}} & \dots & S_{SLC}(k, x)_{M_{\{1,N_D\}}} \end{bmatrix} \quad (\text{A4})$$

for $N_D \in \mathbb{N}$,

and for the slave, the following large-matrix is presented:

$$S_{SLC}(k, x)_S = \begin{bmatrix} S_{SLC}(k, x)_{S_{\{1,1\}}} & S_{SLC}(k, x)_{S_{\{1,2\}}} & S_{SLC}(k, x)_{S_{\{1,3\}}} & \dots & S_{SLC}(k, x)_{S_{\{1,N_D\}}} \end{bmatrix} \quad (\text{A5})$$

for $N_D \in \mathbb{N}$,

The explanation of the chirp-Doppler sub-aperture strategy, represented in Figure 2 is the following: In Figure 2, master and slave sub-bands are generated by focusing the SAR image, where the matched-filter is set to exploit a range-azimuth bandwidth equal to $B_{c_r}, B_{c_D} - B_{D_L}$. The not-processed bandwidths B_{D_L} are divided into N_D equally-distributed bandwidths steps respectively. At this point N_c rigid shifts of the master-slave system are made along the azimuth bandwidth domain, this is made to populate the entire row of Equations (A4) and (A5). The process is repeated N_D times for each shift in azimuth, in fact, Figure 2 (1), (2), and (3), represent the azimuth frequency variation strategy when the Doppler bandwidth is located at N_D . At each Doppler frequency shift $\frac{B_{c_D} - B_{D_L}}{N_D}$ every element of (A4), and (A5) is populated.

Appendix A.3. Doppler Sub-Aperture Strategy

The decomposition of the SAR data into Doppler sub apertures is formalized in this subsection, which is performed starting from the spectral representation of the focused SAR data. To this end, notice that the generic i -th chirp sub-aperture 2-dimensional DFT of (A2) is given by:

$$\begin{aligned} S_{SLC_{F_i}}(n, q) &= DFT2 \left\{ 2N\tau \exp \left[-j \frac{4\pi r}{\lambda} \right] \operatorname{sinc} \left[\pi B_{c_{r_i}} (k - L_{c_g}) \right] \operatorname{sinc} \left[\pi B_{c_D} (x - L_{D_h}) \right] \right\} \\ &= 2N\tau \exp \left[-j \frac{4\pi r}{\lambda} \right] \sum_{k=0}^{N-1} \sum_{x=0}^{M-1} \operatorname{sinc} \left[\pi B_{c_{r_i}} (n - L_{c_g}) \right] \operatorname{sinc} \left[\pi B_{c_D} (q - L_{D_h}) \right] \\ &\quad \exp \left(-j \frac{2\pi kn}{N} \right) \exp \left(-j \frac{2\pi xq}{M} \right) \\ &= 2N\tau \exp \left[-j \frac{4\pi r}{\lambda} \right] \frac{1}{\pi B_{c_{r_i}}} \operatorname{rect} \left[\frac{n}{\pi B_{c_{r_i}}} \right] \frac{1}{\pi B_{c_D}} \operatorname{rect} \left[\frac{q}{\pi B_{c_D}} \right] \exp \left(-j 2\pi n L_{c_g} \right) \exp \left(-j 2\pi q L_{D_h} \right). \end{aligned} \quad (\text{A6})$$

from the last equation, it turns out that a single point stationary target has a two-dimensional rectangular nature with total length proportional to the range-azimuth bandwidths respectively. The phase term $\exp(-j 2\pi n L_{c_g}) \exp(-j 2\pi q L_{D_h})$ is due to the sinc function dislocation in range and azimuth when the SLC SAR data are considered. In the SAR, the movement of a point target with velocity in both range and azimuth direction is immediately warned by the focusing process, resulting in the following anomalies:

- azimuth displacement in the presence of target constant range velocity;
- azimuth smearing in the presence of target azimuth velocity or target range accelerations;
- range-walking phenomenon, visible as range defocusing, in the presence of target range speed, backscattered energy can be detected over one or more range resolution cells.

In practical cases, the backscattered energy from moving targets is distributed over several range-azimuth resolution cells. As a matter of fact, considering the point-like target T_1 (of Figure 1) that is moving with velocity \vec{v}_t whose range-azimuth and acceleration components are $\{v_r, v_a\}$, and $\{a_r, a_a\}$, respectively, then it is possible to highlight

$$\begin{aligned} R^2(t) &= (Vt - S_a)^2 + (R_0 - S_r)^2 \text{ with } S_r = v_r t + \frac{1}{2} a_r t^2 \text{ and } S_a = v_a t + \frac{1}{2} a_a t^2 \\ |R(t)| &= |R_0 - S_r| \left\{ 1 + \frac{(Vt - S_a)^2}{(R_0 - S_r)^2} \right\}^{\frac{1}{2}}. \end{aligned} \quad (\text{A7})$$

considering the following Taylor expansion:

$$(1+x)^\beta \approx 1 + \beta x \quad (\text{A8})$$

and that $R_0 - S_r \approx R_0$, and $(V_t - S_a)^2 \approx V^2 t^2 - 2VtS_a$, (A7) can be written in the following form:

$$|R(t)| = \left\{ |R_0 - S_r| + \frac{1}{2} \frac{(Vt - S_a)^2}{(R_0 - S_r)} \right\} = |R_0 - S_r| + \frac{V^2 t^2}{2R_0} \left(1 - \frac{2S_a}{Vt} \right) \quad (\text{A9})$$

$$\begin{aligned} &= R_0 - S_r + \frac{V^2 t^2}{2R_0} - \frac{Vt S_a}{R_0} = R_0 - v_r t - \frac{1}{2} a_r t^2 + \frac{V^2 t^2}{2R_0} - \frac{Vt \left(v_a t + \frac{1}{2} a_a t^2 \right)}{R_0} \\ &= R_0 - v_r t - \frac{1}{2} a_r t^2 + \frac{V^2 t^2}{2R_0} - \frac{Vv_a t^2}{R_0} - \frac{Va_a t^3}{2R_0}. \end{aligned} \quad (\text{A10})$$

the term $\frac{Va_a t^3}{2R_0}$ can be neglected and by approximating $(V^2 - 2Vv_a) \approx (V - v_a)^2$ Equation (A10) can be written like:

$$|R(Vt)| = R_0 - v_r t + \frac{t^2}{2R_0} \left[(V - v_a)^2 - R_0 a_r \right]. \quad (\text{A11})$$

recasting (A11) in terms of $x = Vt$, We obtain [32]:

$$|R(x)| = R_0 - \epsilon_{r_1} x + \left[(1 - \epsilon_{c_1})^2 - \epsilon_{r_2} \right] \frac{x^2}{2R_0}, \quad x = Vt. \quad (\text{A12})$$

where:

- $\epsilon_{r_1} = \frac{v_r}{V}$ (due to range velocity);
- $\epsilon_{r_2} = \frac{a_r R_0}{V^2}$ (due to range acceleration);
- $\epsilon_{c_1} = \frac{v_c}{V}$ (due to azimuth velocity).

Thus, the above terms modify the received signal, as shown in [32], and should be taken into account in Equation (A6).

References

1. Moe, N.J. *The View from Vesuvius*; University of California Press: Berkeley, CA, USA, 2002.
2. Sigurdsson, H.; Cashdollar, S.; Sparks, S.R. The eruption of Vesuvius in AD 79: Reconstruction from historical and volcanological evidence. *Am. J. Archaeol.* **1982**, *86*, 39–51. [[CrossRef](#)]
3. Papale, P.; Dobran, F. Modeling of the ascent of magma during the plinian eruption of Vesuvius in AD 79. *J. Volcanol. Geotherm. Res.* **1993**, *58*, 101–132. [[CrossRef](#)]
4. Santacroce, R. A general model for the behavior of the Somma-Vesuvius volcanic complex. *J. Volcanol. Geotherm. Res.* **1983**, *17*, 237–248. [[CrossRef](#)]
5. Auger, E.; Gasparini, P.; Virieux, J.; Zollo, A. Seismic evidence of an extended magmatic sill under Mt. Vesuvius. *Science* **2001**, *294*, 1510–1512. [[CrossRef](#)] [[PubMed](#)]
6. De Natale, G.; Troise, C.; Trigila, R.; Dolfi, D.; Chiarabba, C. Seismicity and 3-D substructure at Somma–Vesuvius volcano: evidence for magma quenching. *Earth Planet. Sci. Lett.* **2004**, *221*, 181–196. [[CrossRef](#)]
7. De Lorenzo, S.; Di Renzo, V.; Civetta, L.; D’antonio, M.; Gasparini, P. Thermal model of the Vesuvius magma chamber. *Geophys. Res. Lett.* **2006**, *33*, 16. [[CrossRef](#)]
8. Zuccaro, G.; Cacace, F.; Spence, R.; Baxter, P. Impact of explosive eruption scenarios at Vesuvius. *J. Volcanol. Geotherm. Res.* **2008**, *178*, 416–453. [[CrossRef](#)]
9. Benkhelifa, M.; Gindre, M.; Le Huerou, J.Y.; Urbach, W. Echography using correlation techniques: Choice of coding signal. *IEEE Trans. Ultrason. Ferroelectr. Freq. Control.* **1994**, *41*, 579–587. [[CrossRef](#)]
10. Carotenuto, R.; Caliano, G.; Caronti, A.; Savoia, A.; Pappalardo, M. Fast scanning probe for ophthalmic echography using an ultrasound motor. *IEEE Trans. Ultrason. Ferroelectr. Freq. Control.* **2005**, *52*, 2039–2046. [[CrossRef](#)]
11. Matani, A.; Shigeno, T. Phase series echography with prior waveform distortion for evaluating posterior waveform distortion. *IEEE Trans. Ultrason. Ferroelectr. Freq. Control.* **2006**, *53*, 2019–2025. [[CrossRef](#)]

12. Anantrasirichai, N.; Hayes, W.; Allinovi, M.; Bull, D.; Achim, A. Line detection as an inverse problem: Application to lung ultrasound imaging. *IEEE Trans. Med. Imaging* **2017**, *36*, 2045–2056. [[CrossRef](#)]
13. Demi, L.; Demi, M.; Prediletto, R.; Soldati, G. Real-time multi-frequency ultrasound imaging for quantitative lung ultrasound—first clinical results. *J. Acoust. Soc. Am.* **2020**, *148*, 998–1006. [[CrossRef](#)]
14. Berryman, J.G. Weighted least-squares criteria for seismic travelttime tomography. *IEEE Trans. Geosci. Remote. Sens.* **1989**, *27*, 302–309. [[CrossRef](#)]
15. Song, L.p.; Zhang, S.y. Singular value decomposition-based reconstruction algorithm for seismic travelttime tomography. *IEEE Trans. Image Process.* **1999**, *8*, 1152–1154. [[CrossRef](#)]
16. Shapiro, N.M.; Campillo, M.; Stehly, L.; Ritzwoller, M.H. High-resolution surface-wave tomography from ambient seismic noise. *Science* **2005**, *307*, 1615–1618. [[CrossRef](#)]
17. Brenguier, F.; Shapiro, N.M.; Campillo, M.; Ferrazzini, V.; Duputel, Z.; Coutant, O.; Nercessian, A. Towards forecasting volcanic eruptions using seismic noise. *Nat. Geosci.* **2008**, *1*, 126–130. [[CrossRef](#)]
18. Devaney, A. Geophysical diffraction tomography. *IEEE Trans. Geosci. Remote. Sens.* **1984**, *1*, 3–13. [[CrossRef](#)]
19. Witten, A.J.; Long, E. Shallow applications of geophysical diffraction tomography. *IEEE Trans. Geosci. Remote. Sens.* **1986**, *24*, 654–662. [[CrossRef](#)]
20. Paulatto, M.; Minshull, T.; Baptie, B.; Dean, S.; Hammond, J.O.; Henstock, T.; Kenedi, C.; Kiddle, E.; Malin, P.; Peirce, C.; et al. Upper crustal structure of an active volcano from refraction/reflection tomography, Montserrat, Lesser Antilles. *Geophys. J. Int.* **2010**, *180*, 685–696. [[CrossRef](#)]
21. Liu, Z.; Chatzidakis, S.; Scaglione, J.M.; Liao, C.; Yang, H.; Hayward, J.P. Muon tracing and image reconstruction algorithms for cosmic ray muon computed tomography. *IEEE Trans. Image Process.* **2018**, *28*, 426–435. [[CrossRef](#)]
22. Sherburn, S.; White, R.S.; Chadwick, M. Three-dimensional tomographic imaging of the Taranaki volcanoes, New Zealand. *Geophys. J. Int.* **2006**, *166*, 957–969. [[CrossRef](#)]
23. Lee, S.J.; Kim, S.; Rhie, J.; Kang, T.S.; Kim, Y. Upper crustal shear wave velocity and radial anisotropy beneath Jeju Island volcanoes from ambient noise tomography. *Geophys. J. Int.* **2021**, *225*, 1332–1348. [[CrossRef](#)]
24. Yudistira, T.; Métaxian, J.P.; Putriastuti, M.; Widiyantoro, S.; Rawlinson, N.; Beauducel, F.; Zulfakriza, Z.; Nugraha, A.; Laurin, A.; Fahmi, A.; et al. Imaging of a magma system beneath the Merapi Volcano complex, Indonesia, using ambient seismic noise tomography. *Geophys. J. Int.* **2021**, *226*, 511–523. [[CrossRef](#)]
25. Letort, J.; Roux, P.; Vandemeulebrouck, J.; Coutant, O.; Cros, E.; Wathelet, M.; Cardellini, C.; Avino, R. High-resolution shallow seismic tomography of a hydrothermal area: Application to the Solfatara, Pozzuoli. *Geophys. J. Int.* **2012**, *189*, 1725–1733. [[CrossRef](#)]
26. Agostinetti, N.P.; Chiarabba, C. Seismic structure beneath Mt Vesuvius from receiver function analysis and local earthquakes tomography: Evidences for location and geometry of the magma chamber. *Geophys. J. Int.* **2008**, *175*, 1298–1308. [[CrossRef](#)]
27. Troiano, A.; Petrillo, Z.; Di Giuseppe, M.G.; Balasco, M.; Diaferia, I.; Di Fiore, B.; Siniscalchi, A.; Patella, D. About the shallow resistivity structure of Vesuvius volcano. *Ann. Geophys.* **2008**, *1*, 1–10. [[CrossRef](#)]
28. Biondi, F.; Addabbo, P.; Clemente, C.; Ullo, S.L.; Orlando, D. Monitoring of Critical Infrastructures by Micromotion Estimation: The Mosul Dam Destabilization. *IEEE J. Sel. Top. Appl. Earth Obs. Remote. Sens.* **2020**, *13*, 6337–6351. [[CrossRef](#)]
29. Biondi, F.; Addabbo, P.; Ullo, S.L.; Clemente, C.; Orlando, D. Perspectives on the structural health monitoring of bridges by synthetic aperture radar. *Remote. Sens.* **2020**, *12*, 3852. [[CrossRef](#)]
30. Biondi, F. COSMO-SkyMed staring spotlight SAR data for micro-motion and inclination angle estimation of ships by pixel tracking and convex optimization. *Remote. Sens.* **2019**, *11*, 766.
31. Biondi, F.; Addabbo, P.; Orlando, D.; Clemente, C. Micro-motion estimation of maritime targets using pixel tracking in COSMO-SkyMed synthetic aperture radar data—An operative assessment. *Remote. Sens.* **2019**, *11*, 1637. [[CrossRef](#)]
32. Raney, R.K. Synthetic Aperture Imaging Radar and Moving Targets. *IEEE Trans. Aerosp. Electron. Syst.* **1971**, *3*, 499–505. [[CrossRef](#)]
33. Tufillaro, N.B. Nonlinear and chaotic string vibrations. *Am. J. Phys.* **1989**, *57*, 408–414. [[CrossRef](#)]
34. Biondi, F.; Clemente, C.; Orlando, D. An Atmospheric Phase Screen Estimation Strategy Based on Multichromatic Analysis for Differential Interferometric Synthetic Aperture Radar. *IEEE Trans. Geosci. Remote. Sens.* **2019**, *57*, 7269–7280. [[CrossRef](#)]
35. Curlander, J.C.; McDonough, R.N. *Synthetic Aperture Radar: Systems and Signal Processing*; Wiley: New York, NY, USA, 1991.